COMMUNICATION

Check for updates

Solvation regulation and interfacial adsorption by ethanolamine-based eutectic electrolytes toward byproduct-free zinc anodes

Mengya Wang, Haonan Zheng, Hui Zhang, Gaorong Han, Wei-Qiang Han [ID] and Hangjun Ying [ID] *

This study designs ethanolamine-based hydrated eutectic electrolytes to stabilize Zn anodes by coregulating the solvation structure and interfacial adsorption. EA interacts with Zn^{2+} to suppress H_2O and anion (OTf^-) coordination, and it preferentially anchors on the Zn anode. Therefore, a superior lifespan of Zn||Zn cells of over 1800 h at 2 mA cm^{-2}/2 mAh cm^{-2} and enhanced stability of an active carbon cathode are obtained.

Aqueous Zn anode-based energy storage devices have received broad attention for their intrinsic safety, abundant resources, low standard potential (−0.76 V *vs.* SHE), and high theoretical capacities (820 mAh g^{-1}, 5855 mAh L^{-1}).[1] However, dendrite growth originating from unlimited two-dimensional (2D) Zn^{2+} diffusion and water-induced parasitic reactions arising from abundant water in a free or coordinated state confine the application of Zn anodes. Featuring high tunability, superior dissolution ability, and favorable thermal/electrochemical stability, eutectic electrolytes can resolve the above-mentioned problems.[2] By virtue of hydrogen-bond interactions in the eutectic network, Grotthuss-mediated proton transfer and the hydrogen evolution reaction (HER) can be inhibited.[3] Meanwhile, the introduced organic ligands can coordinate with Zn^{2+} through Lewis acid–base interactions and generate an adsorption layer on the Zn anode, thereby tuning interfacial phenomena like the solid–electrolyte interphase (SEI) and electric double layer (EDL).

The inherent high viscosity of deep eutectic solvents (DESs) gives rise to the large overpotential of eutectic electrolytes, promoting research into hydrated eutectic electrolytes (HEEs). Generally, substituting solid ligands like urea[4] and acetamide[5] with liquid ones[6] can promote the ionic dissociation of zinc salts. Meanwhile, applying zinc salts with a high dissociation ability, like $Zn(OTf)_2$, also contributes to higher ionic conductivity. For example, multiple alcohol molecules, like 2-propanol,[7] ethylene glycol,[8] and 1,3-propanediol,[9] are incorporated into

School of Materials Science and Engineering, Zhejiang University, Hangzhou 310027, China. E-mail: yinghangjun@zju.edu.cn

$Zn(OTf)_2$-based HEEs for commendable bulk mass transfer with confined water activity. Similarly, amino alcohols with bifunctional groups of –OH and –NH_2 exhibit high polarity for interfacial adsorption and are conducive for tuning Zn^{2+} coordination structures.[10,11]

Herein, we construct ethanolamine (EA)-based HEEs with highly dissociated $Zn(OTf)_2$, in which the solvation structure and interfacial chemistry are modified for a byproduct-free Zn anode. EA interacts with H_2O through hydrogen bond interactions, and it participates in the Zn^{2+} solvation shell for reduced H_2O and OTf^- coordination. In addition, boosted by the preferential adsorption of EA molecules, EA-based HEEs manifest an interface where Zn^{2+} is aggregated and OTf^- is excluded for enhanced EDL capacitance and promoted interfacial kinetics. Consequently, a clear Zn anode surface without an OTf^--derived interphase is obtained, which inhibits parasitic reactions. Zn||Zn cells deliver a prolonged lifespan of 1800 h at 2 mA cm^{-2}/2 mAh cm^{-2}. When paired with an active carbon cathode, EA-based HEEs render a higher discharge capacity with capacity retention of 85% for 5000 cycles, and deliver favorable low-temperature performance at −20 °C.

Electrostatic potential (ESP) maps of H_2O and EA molecules are shown in Fig. 1a. H_2O displays a bipolar nature. EA is an amino alcohol and contains the two distinctive functional groups of –OH and –NH_2.[12,13] As EA is miscible with water in all proportions,[14] here, we mix H_2O with EA at different volume ratios and fix the content of $Zn(OTf)_2$ at 1 M (mol L^{-1}), denoting 1 M $Zn(OTf)_2$ in H_2O:EA = 3:2 as HE32 electrolyte. Upon increasing the water content, the viscosity of HEEs decreases from 38.4 mPa s for HE14 to 5.4 mPa s for HE32, and the ionic conductivity increases from 2.6 mS cm^{-2} to 13.3 mS cm^{-2}, suggesting more complete salt dissolution in HE32 (Fig. 1b). In terms of electrolyte performance, Zn||Zn cells with HE32 deliver the longest lifespan of 1800 h at 1 mA cm^{-2}/1 mAh cm^{-2}, combined with a comparable overpotential with $Zn(OTf)_2$ electrolyte (Fig. S1, SI). In the ''reservoir half-cell'' galvanostatic protocol, Zn||Cu cells with HE32 deliver a higher
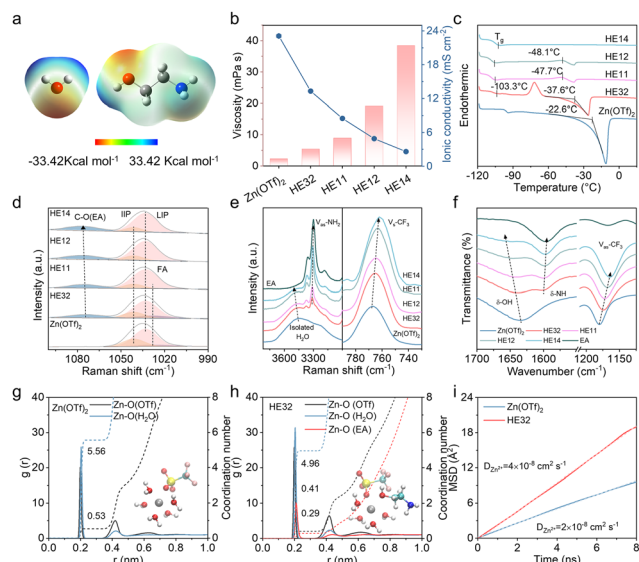
Fig. 1 The physicochemical performance and chemical coordination environment. (a) ESP maps. (b) Viscosity and ionic conductivity. (c) DSC curves. (d, e) Raman and (f) FT-IR spectra. Radial distribution functions (RDFs) and primary solvation sheaths (PSSs) of (g) $Zn(OTf)_2$ and (h) HE32 electrolytes. (i) MSD functions of Zn^{2+}.

average CE of 98.5% with a steady voltage profile, confirming the optimal performance of HE32 electrolyte (Fig. S2, SI). Differential scanning calorimetry (DSC) shows that in the cooling process, the freezing point is greatly reduced from $Zn(OTf)_2$ (-27.3 °C) to HE32 electrolyte (-49.2 °C) (Fig. S3, SI). With lower water content, the melting point reduces, and the exothermic peak weakens (Fig. 1c). The consistent glass transition temperature of HEEs below -100 °C validates the formation of DESs.

Furthermore, the chemical coordination in electrolytes is analyzed via spectral characterization and molecular dynamics (MD) simulations (Figs S4 and S5, Table S1, SI). As shown in Fig. 1d, the symmetric stretching vibration of SO_3 can be deconvoluted into three peaks: free anions (FAs, 1028 cm^{-1}), loose ion pairs (LIPs, 1033 cm^{-1}), and intimate ion pairs (IIPs, 1041 cm^{-1}).[8] HE14, HE12, and HE11 nearly contain no FAs, while HE32 shows more FAs and LIPs than $Zn(OTf)_2$, implying favored salt dissolution in HE32. With increasing EA content, the stretching vibration of C–O at 1703 cm^{-1} shifts positively, while the interaction of C–O with Zn^{2+} at 1468 cm^{-1} undergoes a red shift, suggesting the strengthened coordination of EA to Zn^{2+} (Fig. S7a, SI).[15] Meanwhile, the isolated water clusters undergo a blue shift due to hydrogen bonding interactions with EA molecules, as evidenced by the redshifting of the asymmetric stretching vibration of NH_2 at 3310 cm^{-1} (Fig. 1e). The hydrogen bond number obtained from MD simulations also validates the interaction of EA and H_2O, with decreased H_2O-H_2O interactions (Fig. S6, SI). The symmetric stretching vibration of CF_3 at 766 cm^{-1} experiences a red shift, suggesting a shortened C–F bond length and stabilized OTf$^-$ anions in HEEs. These findings are in line with the Fourier-transform infrared (FT-IR) spectroscopy results (Fig. 1f and Fig. S7b, SI).[16,17]

MD simulation results are presented in Fig. 1g and h. $Zn(OTf)_2$ electrolyte delivers a nearly fully hydrated solvation

shell with 5.56 H_2O and 0.53 OTf$^-$ participating. However, in HE32 electrolyte, EA, with a higher electron-donating ability than H_2O, reduces the number of solvated H_2O and OTf$^-$ anions, giving rise to a solvation structure of $Zn(H_2O)_{4.96}$-$(OTf)_{0.41}(EA)_{0.29}^{1.59+}$. The lower hydration degree of Zn^{2+} in HE32 electrolyte decreases water activity and contributes to promoting bulk Zn^{2+} transfer. According to the mean square displacement (MSD) of Zn^{2+}, HE32 electrolyte displays a higher self-diffusion coefficient of 4×10^{-8} cm^2 s^{-1} than $Zn(OTf)_2$ electrolyte (2×10^{-8} cm^2 s^{-1}) (Fig. 1i). The Zn^{2+} transference number in HE32 electrolyte also shows a larger value of 0.39 than in $Zn(OTf)_2$ electrolyte (0.11) (Fig. S8, SI), validating the promoted Zn^{2+} diffusion in EA-based HEEs.

With regard to interfacial behavior, the bifunctional groups in EA will provide multiple anchor sites on the Zn anode. EA demonstrates a higher-energy highest occupied molecular orbital (HOMO) and lower-energy lowest unoccupied molecular orbital (LUMO) than H_2O, suggesting easier electron exchange between EA and Zn metal (Fig. 2a).[18] Consequently, EA molecules show a larger adsorption energy of -2.31 eV than H_2O (-0.28 eV), verifying the preferential adsorption behavior of EA on the Zn metal surface (Fig. 2b).[4] To monitor the interfacial EDL structure, EDL capacitance in the non-faradaic region and differential capacitance (DC) obtained by impedance-potential testing are measured. The fitted EDL capacitance of Zn||Zn cells in HE32 is about 30 times higher than that in $Zn(OTf)_2$ electrolyte (2993 µF cm^{-2} vs. 92 µF cm^{-2}) (Fig. 2c and Fig. S9, SI). Based on the equation $C = \epsilon A/d$, the increase in C (EDL capacitance) implies an increase in A (electrode effective surface area) and a decrease in d (EDL thickness).[19] The DC values obtained from Zn||Cu cells manifest an identical tendency: HE32 shows higher values in the range of 0.2–0.6 V (Fig. 2d). As
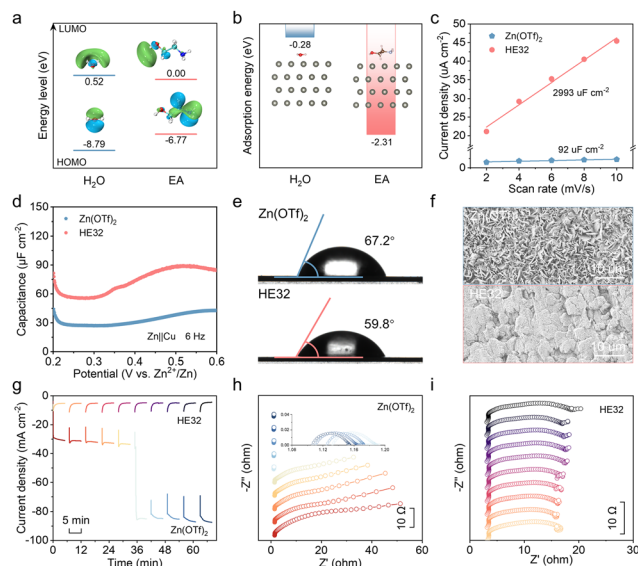

Fig. 2 Preferential adsorption behavior and interface stability. (a) HOMO/LUMO energy levels and (b) adsorption energies on the Zn (002) plane. (c) EDL capacitances of Zn||Zn cells. (d) DCs of Zn||Cu cells. (e) Contact angles. (f) SEM images of Zn anodes saturated for 48 h. Sequential CA curves and EIS plots in (g) $Zn(OTf)_2$ and (i) HE32 electrolytes.

DC reflects the total charge of ions adsorbed on the Zn anode surface, higher DC in HE32 electrolyte suggests the exclusion of OTf^- at the electrode–electrolyte interface, reducing parasitic reactions, and the aggregation of Zn^{2+} for dense and homogeneous Zn^{2+} deposition.[20]

In contact angle measurements, HE32 electrolyte shows a lower contact angle on the Zn anode than $Zn(OTf)_2$ electrolyte ($59.8°$ vs. $67.2°$) (Fig. 2e). The promoted wettability and hydrophilicity in HE32 electrolyte help to guide smooth Zn deposition. After saturation for 48 h, the Zn anode in HE32 electrolyte delivers a compact surface. However, in $Zn(OTf)_2$ electrolyte, the Zn anode is covered by massive irregular byproducts, and the effective surface area of the Zn anode is accordingly decreased (Fig. 2f).

Fig. S10, SI, reveals the chronoamperometry (CA) curves, where $Zn(OTf)_2$ electrolyte shows continuously increased current density and apparent Zn^{2+} 2D diffusion. Sequentially coupled CA and electrochemical impedance spectroscopy (EIS) measurements were applied to investigate the Zn^{2+} deposition behavior. CA in $Zn(OTf)_2$ electrolyte exhibits a larger current response in total and experiences a sharp decrease (Fig. 2g). As elucidated by EIS plots, due to unrestricted Zn^{2+} 2D diffusion to easy deposition sites, protrusions grow gradually, the interfacial impedance decreases, and short circuits occur (Fig. 2h). However, in HE32, the current density stabilizes quickly upon the start of CA testing, indicating well-regulated Zn^{2+} 3D diffusion by the EA adsorption layer. Afterwards, Zn||Zn cells exhibit nearly identical CA plots, and the EIS curves remain steady throughout the deposition process, verifying the consistent uniform deposition (Fig. 2i).

In terms of interfacial kinetics, HE32 delivers incredibly smaller charge transfer resistance (R_{ct}), and the activation energy decreases to 38.94 kJ mol^{-1}, lower than that of $Zn(OTf)_2$ (50.83 kJ mol^{-1}) (Fig. 3a, Fig. S11, SI). The promoted EDL capacitance and enhanced wettability in HE32 help to accelerate the interfacial dynamics. In addition, $Zn(OTf)_2$ electrolyte exhibits larger yet more volatile CV curves, implying rapid mass transfer and a volatile interface in aqueous electrolyte (Fig. 3b and c). The consistent CV curves in HE32 verify that a stable interface is generated at first and is sustained over repeat cycles (Fig. S12, SI).

Tafel plots reflect a much lower corrosion current density of 2.02 mA cm^{-2} in HE32 electrolyte (Fig. 3d). After 50 cycles, the Zn anode in HE32 exhibits no parasitic products of the form $Zn_x(OTf)_y(OH)_{2x-y}\cdot nH_2O$, and shows a higher tendency for Zn (002) growth ($I_{(002)/(100)} = 2.35$) (Fig. 3e).[21] Conversely, $Zn(OTf)_2$ electrolyte manifests a higher corrosion current density of 3.07 mA cm^{-2}, and the cycled Zn anode shows multiple signals from byproducts.

The XPS spectrum of the cycled Zn anode in HE32 exhibits a higher content of C–O/C–N, confirming the adsorption of EA molecules (Fig. 3f). Meanwhile, the C 1s spectrum shows no signal from CF_3, and the F 1s and S 2p spectra manifest quite weak peaks, fully verifying the exclusion of H_2O and OTf^- from the Zn surface (Fig. 3g and h). The negatively shifted Zn 2p peak in HE32 electrolyte also implies fewer generated byproducts (Fig. S13, SI). However, in $Zn(OTf)_2$ electrolyte, desolvated and
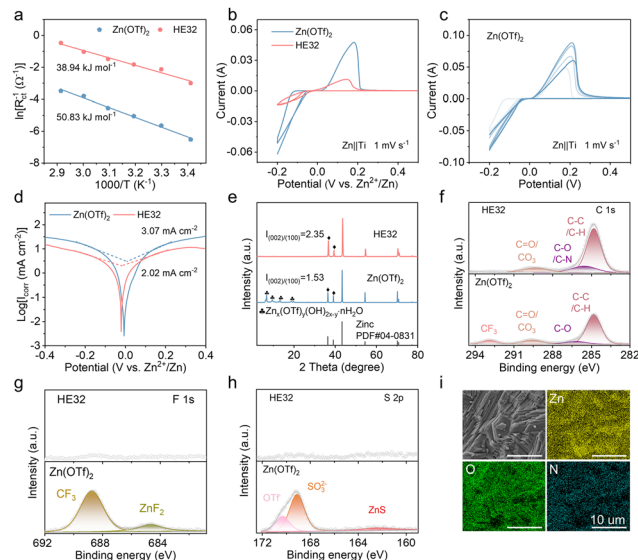

Fig. 3 Interfacial dynamics and component analysis. (a) Activation energies. (b) The first CV cycles of Zn||Ti cells at 1 mV s^{-1} and (c) CV curves for 5 cycles in $Zn(OTf)_2$ electrolyte. (d) Tafel plots of Zn||Zn cells. (e) XRD patterns of cycled Zn anodes and (f) C 1s, (g) F 1s, and (h) S 2p XPS fine spectra. (i) SEM images and mapping results of a cycled Zn anode in HE32.

interfacially adsorbed OTf^- anions will experience reduction and generate massive mossy byproducts like $Zn_x(OTf)_y(OH)_{2x-y}\cdot nH_2O$, ZnF_2, and ZnS. SEM images of the cycled Zn anode in HE32 show a compact deposition morphology (Fig. 3i). The uniform distribution of Zn, O, and N elements indicates the beneficial effect of the EA adsorption layer for even Zn^{2+} deposition. The energy spectra and element proportions given in Fig. S14, SI, also validate the absence of F and S elements on the Zn metal surface.

To confirm the practicability of HE32 electrolyte, the electrochemical performances of Zn||Zn and Zn||Cu cells, and full batteries paired with active carbon (AC), are evaluated. Due to enhanced interfacial kinetics, Zn||Zn cells in HE32 show drastically decreased R_{ct} under open-circuit conditions and after 50 cycles (Fig. 4a and Fig. S15, SI). Fig. 4b shows the cycling performance of Zn||Zn cells at 2 mA cm^{-2}/2 mAh cm^{-2}. The cell in $Zn(OTf)_2$ electrolyte undergoes rapid short-circuiting. HE32 electrolyte enables the steady operation of a Zn||Zn cell for 1800 h, and the overpotential is comparable with that in aqueous solution (Fig. S16, SI). In terms of rate performance, HE32 operates normally from 0.2 mA cm^{-2} to 3 mA cm^{-2}, and the overpotential reduces slightly (Fig. 4c). However, in $Zn(OTf)_2$ electrolyte, Zn||Zn cells malfunction during the second 0.5 mA cm^{-2} step. The cycled Zn anode in $Zn(OTf)_2$ is mossy and irregular, full of loose byproducts, while the Zn anode in HE32 displays compact morphology with a (002) orientation (Fig. 4d).

Zn||Cu cells with HE32 electrolyte operate steadily at 1 mA cm^{-2} for 2000 cycles and the average CE is 99.41%, higher than the chaotic distribution in $Zn(OTf)_2$ (Fig. 4e). The corresponding voltage profiles present better consistency in HE32 (Fig. 4f). In HE32 electrolyte, the enhanced wettability toward the AC cathode (Fig. S17, SI), the dramatically low
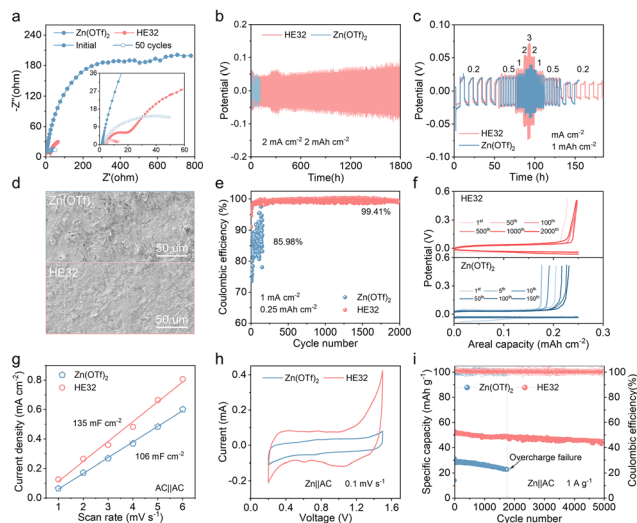
Fig. 4 The electrochemical performance of electrolytes. (a) Nyquist plots of Zn||Zn cells. (b) Cyclic performance of Zn||Zn cells. (c) Rate performance. (d) SEM images of cycled Zn anodes. (e) CEs and (f) voltage profiles of Zn||Cu cells. (g) EDL capacitance of AC||AC cells. (h) CV curves and (i) cyclic performance of Zn||AC cells.

interfacial impedance (R_{inter}) and R_{ct} values (Fig. S18, SI), and the larger EDL capacitance of the AC cathode (Fig. 4g and Fig. S19, SI) contribute to improved energy storage. Larger-area CV curves are observed in HE32 electrolyte (Fig. 4h). Therefore, HE32 electrolyte delivers an initial discharge capacity of 53 mAh g^{-1}, and achieves capacity retention of 85% for 5000 cycles at 1 A g^{-1} (Fig. 4I and Fig. S20, SI). At different rates, HE32 electrolyte enables higher capacities (Fig. S21, SI). Assisted by the low freezing point, HE32 electrolyte remains stable at -20 °C and renders steady operation at 0.1 A g^{-1} for 100 cycles (Figs. S22 and S23, SI).

In conclusion, we design EA-based HEEs with highly dissociated Zn(OTf)$_2$, achieving a byproduct-free Zn anode through coregulating the solvation structure and interfacial adsorption. EA with –OH and –NH$_2$ confines water in a eutectic network *via* hydrogen bond interactions, and reduces the content of solvated H$_2$O and OTf$^-$ by Lewis acid–base interactions with Zn^{2+}. In addition, the preferential adsorption of EA on the Zn anode induces an interface where Zn^{2+} is aggregated, while H$_2$O and OTf$^-$ are repelled for enhanced EDL capacitance and interfacial kinetics. Consequently, a clear Zn anode surface without apparent OTf$^-$ reduction is achieved for inhibited side reactions. Zn||Zn cells show a superior lifespan of 1800 h at 2 mA cm^{-2}/2 mAh cm^{-2}. Zn||AC full batteries deliver a capacity retention of 85% for 5000 cycles at 1 A g^{-1}, and enable steady operation at -20 °C. This work provides insights into modulating Zn^{2+} coordination structures and interfacial adsorption for enhanced metal-anode interfacial stability.

Conflicts of interest

There are no conflicts to declare.

Data availability

The data supporting this article have been included as part of the supplementary information (SI). Supplementary information is available. See DOI: https://doi.org/10.1039/d6cc00481d.

References

1 Y. F. Qu, J. W. Qian, F. Zhang, Z. Zhu, Y. Zhu, Z. Hou, Q. Meng, K. Chen, S. X. Dou and L. F. Chen, *Adv. Mater.*, 2024, 2413370.
2 M. Wang, Z. Xu, C. He, L. Cai, H. Zheng, Z. Sun, H. K. Liu, H. Ying and S. Dou, *ACS Nano*, 2025, **19**, 9709–9739.
3 M. Li, Z. Li, X. Wang, J. Meng, X. Liu, B. Wu, C. Han and L. Mai, *Energy Environ. Sci.*, 2021, **14**, 3796–3839.
4 Z. Wang, J. Diao, J. N. Burrow, K. K. Reimund, N. Katyal, G. Henkelman and C. B. Mullins, *Adv. Funct. Mater.*, 2023, **33**, 2304791.
5 S. Wang, S. Chen, Y. Ying, G. Li, H. Wang, K. K. K. Cheung, Q. Meng, H. Huang, L. Ma and J. A. Zapien, *Angew. Chem., Int. Ed.*, 2024, e202316841.
6 D. Wang, H. Peng, S. Zhang, H. Liu, N. Wang and J. Yang, *Angew. Chem., Int. Ed.*, 2023, e202315834.
7 Q. Ma, R. Gao, Y. Liu, H. Dou, Y. Zheng, T. Or, L. Yang, Q. Li, Q. Cu, R. Feng, Z. Zhang, Y. Nie, B. Ren, D. Luo, X. Wang, A. Yu and Z. Chen, *Adv. Mater.*, 2022, **34**, 2207344.
8 R. Chen, C. Zhang, J. Li, Z. Du, F. Guo, W. Zhang, Y. Dai, W. Zong, X. Gao, J. Zhu, Y. Zhao, X. Wang and G. He, *Energy Environ. Sci.*, 2023, **16**, 2540–2549.
9 P. Luo, Y. Wang, W. Zhang, Z. Huang, F. Chao, Y. Yuan, Y. Wang, Y. He, G. Yu, D. Zhu, Z. Wang, H. Tang and Q. An, *Small*, 2025, **21**, 2410946.
10 K. Wang, T. Qiu, L. Lin, H. Zhan, X.-X. Liu and X. Sun, *Energy Storage Mater.*, 2024, **70**, 103516.
11 A. M. Elshahawy, Y. Gao, W. Zhao, J. Li, H. Zhang and X. Liu, *Energy Environ. Mater.*, 2025, **0**, e70151.
12 X. Li, Q. Xu, Z. Liu, J. Chen, H.-B. Xie, S. Chen and J. Liu, *Environ. Sci. Technol.*, 2023, **57**, 9975–9983.
13 A. N. Rose, E. Hettiarachchi and V. H. Grassian, *J. Colloid Interface Sci.*, 2022, **614**, 75–83.
14 Y. P. Klapshin, I. A. Solonina, M. N. Rodnikova, M. R. Kiselev, A. V. Khoroshilov and S. V. Makaev, *Mendeleev Commun.*, 2020, **30**, 534–536.
15 J. Wan, R. Wang, Z. Liu, S. Zhang, J. Hao, J. Mao, H. Li, D. Chao, L. Zhang and C. Zhang, *Adv. Mater.*, 2023, 2310623.
16 J. Wang, H. Qiu, Q. Zhang, X. Ge, J. Zhao, J. Wang, Y. Ma, C. Fan, X. Wang, Z. Chen, G. Li and G. Cui, *Energy Storage Mater.*, 2023, **58**, 9–19.
17 S. Li, Y. Zhong, J. Huang, G. Lai, L. Li, L. Jiang, X. Xu, B. Lu, Y. Liu and J. Zhou, *Energy Environ. Sci.*, 2025, **18**, 2599–2609.
18 K. Wang, H. Zhan, W. Su, X.-X. Liu and X. Sun, *Energy Environ. Sci.*, 2025, **18**, 1398–1407.
19 Y. Chen, Z. Deng, Y. Sun, Y. Li, H. Zhang, G. Li, H. Zeng and X. Wang, *Nano-Micro Lett.*, 2024, **16**, 96.
20 W. Xie, K. Zhu, W. Jiang, H. Yang, M. Ma, L. Zhao and W. Yang, *ACS Nano*, 2024, **18**, 21184–21197.
21 J. Li, S. Qin, M. Xu, W. Wang, J. Zou, Y. Zhang, H. Dou and Z. Chen, *Adv. Funct. Mater.*, 2024, 2402186.